Simultaneous X-Ray and Infrared Observations of Sagittarius A*'s Variability

H. Boyce[1] , D. Haggard[1,2] , G. Witzel[3,4] , S. P. Willner[5] , J. Neilsen[6] , J. L. Hora[5] , S. Markoff[7] , G. Ponti[8],
F. Baganoff[9], E. E. Becklin[3], G. G. Fazio[5], P. Lowrance[10] , M. R. Morris[3] , and H. A. Smith[5]

[1] Department of Physics and McGill Space Institute, McGill University, 3600 University St., Montreal QC, H3A 2T8, Canada; hope.boyce@mail.mcgill.ca
[2] CIFAR Azrieli Global Scholar, Gravity & the Extreme Universe Program, Canadian Institute for Advanced Research, 661 University Ave., Suite 505, Toronto, Ontario M5G 1M1, Canada
[3] University of California, Los Angeles, CA 90095, USA
[4] Max Planck Institute for Radio Astronomy, Bonn, Germany
[5] Center for Astrophysics, Harvard & Smithsonian, 60 Garden St., Cambridge, MA02138, USA
[6] Kavli Institute for Astrophysics & Space Research, MIT, 70 Vassar St., Cambridge, MA 02139, USA
[7] Anton Pannekoek Institute for Astronomy/GRAPPA, University of Amsterdam, 1098 XH Amsterdam, The Netherlands
[8] Max-Planck-Institut für extraterrestrische Physik, Giessenbachstraße, D-85748 Garching, Germany
[9] Massachusetts Institute of Technology, 77 Massachusetts Avenue, 37-555, Cambridge, MA 02139, USA
[10] IPAC-Spitzer, MC 314-6, California Institute of Technology, Pasadena, CA 91125, USA

Abstract

Emission from Sagittarius A* is highly variable at both X-ray and infrared (IR) wavelengths. Observations over the last ∼20 yr have revealed X-ray flares that rise above a quiescent thermal background about once per day, while faint X-ray flares from Sgr A* are undetectable below the constant thermal emission. In contrast, the IR emission of Sgr A* is observed to be continuously variable. Recently, simultaneous observations have indicated a rise in IR flux density around the same time as every distinct X-ray flare, while the opposite is not always true (peaks in the IR emission may not be coincident with an X-ray flare). Characterizing the behavior of these simultaneous X-ray/IR events and measuring any time lag between them can constrain models of Sgr A*'s accretion flow and the flare emission mechanism. Using 100+ hours of data from a coordinated campaign between the *Spitzer Space Telescope* and the *Chandra X-ray Observatory*, we present results of the longest simultaneous IR and X-ray observations of Sgr A* taken to date. The cross-correlation between the IR and X-ray light curves in this unprecedented data set, which includes four modest X-ray/IR flares, indicates that flaring in the X-ray may lead the IR by approximately 10–20 min with 68% confidence. However, the 99.7% confidence interval on the time-lag also includes zero, i.e., the flaring remains statistically consistent with simultaneity. Long-duration and simultaneous multi-wavelength observations of additional bright flares will improve our ability to constrain the flare timing characteristics and emission mechanisms, and must be a priority for Galactic Center observing campaigns.

Key words: accretion, accretion disks – black hole physics – Galaxy: center – radiation mechanisms: non-thermal

1. Introduction

Sagittarius A* (Sgr A*) sits at the center of the Milky Way and is the closest supermassive black hole (SMBH), at a distance of only ∼8 kpc (e.g., Boehle et al. 2016; Gillessen et al. 2017). Monitored in the radio since its discovery, and more recently in the infrared (IR) and the X-ray, Sgr A* has a mass of $\sim 4 \times 10^6\,M_\odot$ (Boehle et al. 2016; Gillessen et al. 2017), an extremely low bolometric-to-Eddington luminosity ratio ($L/L_{\mathrm{Edd}} \sim 10^{-9}$; Genzel et al. 2010), and appears to be accreting material at a very low rate ($\lesssim 10^{-7}\,M_\odot\,\mathrm{yr}^{-1}$; Baganoff et al. 2003; Marrone et al. 2006, 2007; Shcherbakov et al. 2012; Yusef-Zadeh et al. 2015).

In X-rays, Sgr A* appears as a persistent source, with a flux of about $3 \times 10^{33}\,\mathrm{erg\,s^{-1}}$ (Baganoff et al. 2001, 2003). This faint, steady emission arises from thermal bremsstrahlung radiation from a hot accretion flow dominated by regions near the Bondi radius (Quataert 2002; Baganoff et al. 2003; Yuan et al. 2003; Liu et al. 2004; Xu et al. 2006; Wang et al. 2013) and is interrupted about once per day by distinct flares of non-thermal emission coming from very close to the black hole (Neilsen et al. 2013, 2015). First detections of Sgr A* in the IR also revealed a highly variable source (Genzel et al. 2003; Ghez et al. 2004) with peaks in the IR emission detected more frequently than in X-rays. Since these first discoveries, the

statistical behavior of both the X-ray (e.g., Li et al. 2015; Neilsen et al. 2015; Ponti et al. 2015) and the IR (e.g., Dodds-Eden et al. 2011; Witzel et al. 2012, 2018; Hora et al. 2014) activity have been well studied and the flux density distributions of these two wavelengths can both be described by a power law (Witzel et al. 2012, 2018; Neilsen et al. 2015). Though the X-ray and IR have no other clear statistical similarities, the coincidence of peaks in the variability hints that there may be a physical connection between them (e.g., Eckart et al. 2006a, 2008; Yusef-Zadeh et al. 2006, 2009; Dodds-Eden et al. 2009; Mossoux et al. 2016). The picture is even less clear at longer wavelengths, where some submm flares have been tentatively linked to IR flares with some delay (Marrone et al. 2008; Morris et al. 2012) or no delay (Fazio et al. 2018), and radio variability has not been observed to coincide with IR or X-ray activity (e.g., Capellupo et al. 2017). However, upcoming submm and coordinated multi-wavelength observations undertaken by the Event Horizon Telescope collaboration (Doeleman et al. 2008) may shed light on these connections in the near future.

Despite the intensive efforts that have been made to characterize Sgr A*'s variable emission, the physical mechanisms producing the variability are still unknown. Suggested physical models include particle acceleration due to magnetic

reconnection events, violent disk instabilities, jets, other stochastic processes in the accretion flow (e.g., Markoff et al. 2001; Liu & Melia 2002; Yuan et al. 2003; Liu et al. 2004; Dexter et al. 2009; Maitra et al. 2009; Dodds-Eden et al. 2010; Ball et al. 2016; Li et al. 2017), and even tidal disruption of asteroids (Čadevž et al. 2008; Kostić et al. 2009; Zubovas et al. 2012). Additional models attempt to explain the variability in the context of expanding plasma blobs (e.g., van der Laan 1966; Marrone et al. 2008; Younsi & Wu 2015; Li et al. 2017), themselves launched by magnetic reconnection events or unsteady jet emission. Finally, gravitational lensing near the horizon of the SMBH might add an amplifying effect to the observed emission (Chan et al. 2015).

One possible picture for the IR flares describes a population of electrons undergoing continuous acceleration due to turbulent processes in the inner accretion flow and subsequently emitting synchrotron radiation. This is supported by observed timescales for the IR variability, with factors of $\gtrsim 10$ changes within ~ 10 min (e.g., Genzel et al. 2003; Ghez et al. 2004; Witzel et al. 2018), the spectral index at high flux densities ($\alpha \approx 0.6$; Hornstein et al. 2007; Bremer et al. 2011; Witzel et al. 2014), and the high linear polarization of the IR emission (Eckart et al. 2006b, 2008; Meyer et al. 2006, 2007; Trippe et al. 2007; Yusef-Zadeh et al. 2007; Witzel et al. 2011; Shahzamanian et al. 2015). The exact physical parameters of this turbulant acceleration of electrons (e.g., background magnetic field strength and γ, the Lorentz factor of the electrons) and the details of the radiative processes linking the IR flares to the X-ray remain unknown.

The radiation mechanisms often invoked to connect IR flares to simultaneous X-ray outbursts include pure synchrotron (e.g., Markoff et al. 2001; Dodds-Eden et al. 2009; Barrière et al. 2014; Ponti et al. 2017), synchrotron self-Compton (SSC) (Markoff et al. 2001; Eckart et al. 2008), and inverse Compton (IC; Yusef-Zadeh et al. 2012). Monitoring the black hole *simultaneously* in multiple wavelengths can constrain these variability models via the association of peaks at different energies and times. With this motivation, Sgr A* has recently been monitored simultaneously at wavelengths ranging from the radio, mm, submm, IR, X-rays, to gamma-rays (e.g., Dodds-Eden et al. 2009; Yusef-Zadeh et al. 2009, 2006; Trap et al. 2011; Eckart et al. 2012, 2006a; Fazio et al. 2018).

Sgr A*'s flaring radiation mechanisms can also be constrained by the statistical behavior of the flares. For example, Dibi et al. (2016) showed that the measured flux distributions of flares in the X-ray (Neilsen et al. 2013, 2015) and IR (Witzel et al. 2012, 2018) were consistent with both synchrotron and SSC models, though their different shapes are difficult to understand if driven by the same particle populations.

The first simultaneous IR and X-ray observations of Sgr A* were carried out by Eckart et al. (2004). Since then, studies with both X-ray and IR monitoring of Sgr A* have often reported that flares in the two wavelengths are simultaneous with each other or with the X-ray leading the IR by no more than 10 min (Eckart et al. 2006a, 2008; Yusef-Zadeh et al. 2006, 2009; Dodds-Eden et al. 2009; Mossoux et al. 2016). The exception is Yusef-Zadeh et al. (2012), who reported a short time lag between the maxima of the IR and X-ray flares, with the X-ray flares possibly *lagging* the IR. Such a behavior would point toward an interpretation of an IC scattering model, where

a fraction of IR photons are up-scattered to X-ray energies and are seen as an X-ray "echo."

These studies support the inference of a physical connection between the X-ray and IR flaring. However, the ground-based IR observations are often significantly shorter than the X-ray observations and there are frequently gaps in the data. When flares occur in one wavelength outside the observing window of another observatory, it is difficult to robustly associate two events (e.g., Marrone et al. 2008; Mossoux et al. 2016; Capellupo et al. 2017), leading to uncertainty in the cross-correlation.

The first observations of Sgr A* with the *Spitzer Space Telescope* (Hora et al. 2014) provided a continuous >23 hr light curve of Sgr A* at IR wavelengths that was more than a factor of two longer than the previous record holder (600 min; Meyer et al. 2008). Building on this study, we utilized two space telescopes (*Spitzer* and the *Chandra X-ray Observatory*) to obtain six simultaneous observations of Sgr A* at 4.5 μm and 2–8 keV. Four of these epochs have ~ 24 hr of overlapping coverage from the two observatories, maximizing the probability of catching the relatively rare X-ray flares with simultaneous IR monitoring. A detailed statistical analysis of the IR data was presented in Witzel et al. (2018), and our first multi-wavelength results were reported in Fazio et al. (2018).

In this work we investigated the temporal correlations between X-ray and IR variability using these six contemporaneous *Chandra* and *Spitzer* observations of Sgr A*. Section 2 describes these observations and the reduction of the data, while Section 3 details our characterization of the variability of Sgr A* by cross-correlating the light curves. Section 4 explores the results in the context of previous studies and discusses their implications for models of the variability.

2. Observations and Data Reduction

The IRAC instrument (Fazio et al. 2004) on *Spitzer* (Werner et al. 2004) was used to observe Sgr A* at 4.5 μm for eight ~ 24 hr long stretches between 2013 and 2017. Six of these observations had simultaneous monitoring from *Chandra* (Weisskopf et al. 2000), centered on Sgr A*'s radio position (R.A., decl. = 17:45:40.0409, -29:00:28.118; Reid & Brunthaler 2004) and are listed in Table 1. The first two epochs had overlapping *Chandra* coverage for ~ 5.5 hr, while the other four had continuous ~ 24 hr coverage from both observatories. This results in a total of ~ 107 hr for which we collected simultaneous X-ray and IR data—the largest such data set to date. Figure 1 shows the resulting Sgr A* light curves.

2.1. Spitzer

Sgr A* and its immediate surroundings are unresolved with the *Spitzer*/IRAC detector. The measured flux of a single pixel is also highly sensitive to any changes in the telescope's pointing, even on the subpixel level. This makes detecting the intrinsic variability of Sgr A* a significant challenge. Recovering the signal requires modeling the flux variations of the pixel containing the black hole as a property of both (1) the varying intra-pixel sensitivity of *Spitzer*/IRAC detector and (2) the telescope's sub-pixel motion. Hora et al. (2014) presented the first detection of Sgr A* with *Spitzer* and demonstrated that a very precise relative flux measurement can be recovered for Sgr A* using this approach.

Table 1
Observing Log for Simultaneous *Chandra* and *Spitzer* Observations

| Obs Date | Chandra | | | Spitzer | | | |
	ObsID	Obs. Start (UT)[a]	Obs. End (UT)[a]	AORKEY	AOR Start (UT)[a]	AOR End (UT)[a]	Mode[b]
2014 Jun 2	16210	(+1) 02:59:23	(+1) 08:40:34	51040768	22:32:00	22:56:01	Map
				51041024	22:59:37	(+1) 10:39:44	Stare part 1
				51041280	(+1) 10:43:22	(+1) 22:23:28	Stare part 2
2014 Jul 4	16597	20:48:12	(+1) 02:21:32	51344128	13:21:59	13:45:55	Map
				51344384	13:49:37	(+1) 01:29:43	Stare part 1
				51344640	(+1) 01:33:21	(+1) 03:13:27	Stare part 2
2016 Jul 12	18731	18:23:59	(+1) 18:42:51	58115840	18:04:23	18:34:03	Map
				58116352	18:37:45	(+1) 06:37:30	Stare part 1
				58116608	(+1) 06:41:14	(+1) 18:40:58	Stare part 2
2016 Jul 18	18732	12:01:38	(+1) 12:09:00	58116096	11:44:02	12:13:43	Map
				58116864	12:17:25	(+1) 00:17:09	Stare part 1
				58117120	(+1) 00:20:54	(+1) 12:20:38	Stare part 2
2017 Jul 15	19703	22:36:07	(+2) 00:01:34	60651008	22:28:54	22:58:34	Map
				63303680	23:02:17	(+1) 11:02:01	Stare part 1
				63303936	(+1) 11:05:46	(+1) 23:05:30	Stare part 2
2017 Jul 25	19704	22:57:27	(+1) 23:28:30	60651264	22:39:33	23:09:14	Map
				63304192	23:12:57	(+1) 11:12:41	Stare part 1
				63304448	(+1) 11:16:26	(+1) 23:16:10	Stare part 2

Notes.
[a] A (+1) in the start/end time columns indicates the offset of one day from the first date listed in the first column. For example, the first *Chandra* observation began at 02:59:23 on June 3. Times are UTC at the observatory. The time-lag analysis was based on corrected heliocentric times.
[b] Mode of operation (either Map or Stare modes). The "Map" mode was a short operation performed after the initial slew to Sgr A*, while the two "Stare" modes were each ∼12 hr long observations taken with a ∼4 min break between the two.

The *Spitzer* data presented in this work were obtained and reduced using the procedures described by Hora et al. (2014) and Witzel et al. (2018), the latter of which analyzes these and additional *Spitzer* light curves in the context of other IR data sets from Keck and the Very Large Telescope (VLT). As documented in Table 1, each observation was conducted as a set of three Astronomical Observation Requests (AORs). Each epoch followed the same observing sequence: an initial mapping operation performed after the slew to the Sgr A* field followed by two successive staring operations. Each staring operation began by using the "PCRS Peakup" mode to position Sgr A* on the center of pixel (16, 16) in the IRAC subarray. The subarray mode for *Spitzer*/IRAC reads out 64 consecutive images (a "frame set") of a 32×32 pixel region on the IRAC detector. This frame set is known as one basic calibrated data product (BCD), which is the data format downloaded from the *Spitzer* Heritage Archive.[11] Each frame in the frame set is a 0.1 s 32×32 image, so one frame set takes 6.4 s to complete. After converting the pixel intensity into mJy, each frame set was combined into a single 32×32 image referred to as a "6.4 s BCD coadd." Since frame sets were typically separated by 2 s of telescope overheads, this resulted in an observation cadence of approximately 8.4 s.

The data reduction is described in Section 2.1 of Witzel et al. (2018), which is an improved version of the procedure in Appendix A1 of Hora et al. (2014). This procedure corrects for the effect of nearby sources on the measured flux of Sgr A* as the telescope jitters on a sub-pixel basis throughout the observations. The resulting light curves are displayed in Figure 1. The baseline flux density of these IR light curves is unknown, though the value has been inferred to be 1.9 mJy from the cumulative distributions of flux densities of Sgr A* in Witzel et al. (2018). Therefore, the *Spitzer* light curves in Figure 1 plot the excess flux density above 1.9 mJy from pixel (16,16), attributed to Sgr A*'s variability.

2.2. Chandra

All *Chandra* observations were acquired using the ACIS-S3 chip in the FAINT mode with a one-eighth subarray. The small subarray was chosen to avoid photon pileup in any bright flares from Sgr A* and in the nearby magnetar, SGR J1745-2900 (Coti Zelati et al. 2015, 2017). We performed *Chandra* data reduction and analysis with CIAO v4.9 tools[12] (Fruscione et al. 2006) and calibration database 4.7.3. The chandra_repro script was used to reprocess level 2 events files before the WCS coordinate system was updated (wcs_update). We used the CIAO tool axbary to apply barycentric corrections to the event times. Finally, we extracted a 2–8 keV light curve from a circular region of radius $1''25$ centered on Sgr A*. The small extraction region and energy range isolate Sgr A*'s emission from the nearby magnetar (e.g., Coti Zelati et al. 2017) and the diffuse X-ray background (e.g., Baganoff et al. 2003; Nowak et al. 2012; Wang et al. 2013). These X-ray light curves are plotted in Figure 1.

---

[11] The *Spitzer* Heritage Archive (http://irsa.ipac.caltech.edu) is part of the NASA/ IPAC Infrared Science Archive, which is operated by the Jet Propulsion Laboratory, California Institute of Technology, under contract with the National Aeronautics and Space Administration.

[12] *Chandra* Interactive Analysis of Observations (CIAO) software is available at http://cxc.harvard.edu/ciao/.
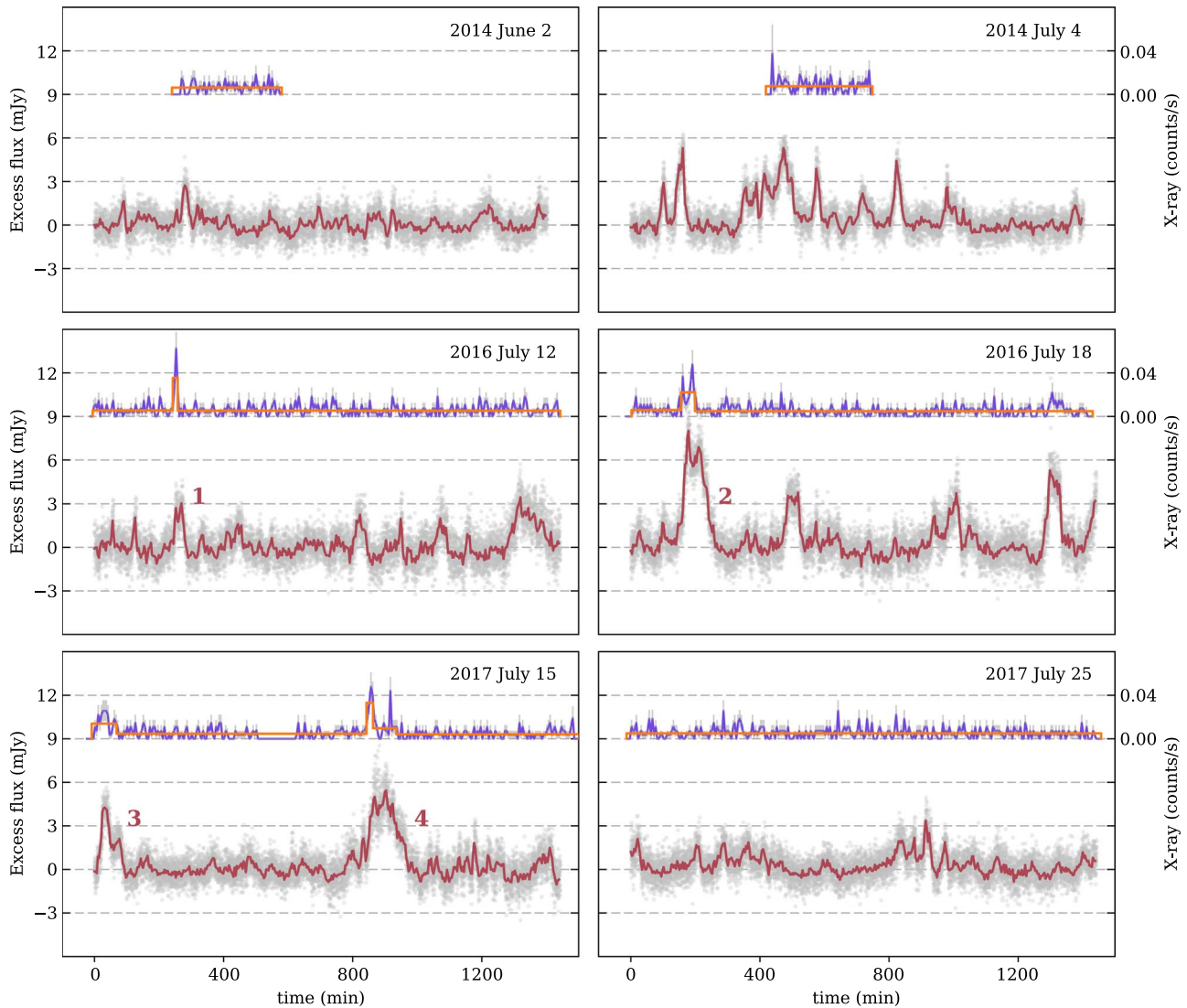
Figure 1. Simultaneous IR and X-ray light curves of Sgr A*. Plotted in gray/red is the excess flux density (mJy) of the pixel containing Sgr A* from *Spitzer* 4.5 μm observations (see Section 2.1 of Witzel et al. 2018). Times for each epoch are relative to the beginning of the *Spitzer* observations, measured in Heliocentric Modified Julian Date. Gray dots are the flux densities of each 6.4 s BCD coadd, while the red line shows the data binned over 3.5 min. *Chandra* light curves of Sgr A* at 2–8 keV are plotted in purple with 300 s binning. The $p_0 = 0.05$ Bayesian Blocks results are overplotted on the X-ray curves in orange. Labels 1–4 indicate the four IR flux peaks associated with significant X-ray activity.

3. Analysis

3.1. Flare Detection and Characteristics

To detect and characterize X-ray flares, we used the Bayesian Blocks algorithm as described by Scargle (1998) and Scargle et al. (2013) and provided by Peter K. G. Williams (bblocks; Williams et al. 2017). This algorithm takes an unbinned, filtered *Chandra* events file as input and models the light curve as a sequence of blocks with constant rates. A single block characterizes a region of the light curve for which there is no significant variability, and a light curve with a flare is made up of multiple blocks of differing count rates separated by change points. The code adopts a geometric prior on the number of blocks, preventing over-fitting the light curve by favoring fewer blocks when fewer events are present in the *Chandra* events file. We ran the algorithm requiring a detection significance of 95% for a single change point (a false positive rate of $p_0 = 0.05$), which implies that the overall detection significance of a flare (at least two change points) is

$1 - p_0^2 \simeq 99.8\%$ (see, e.g., Nowak et al. 2012; Neilsen et al. 2013).

We detected four X-ray flares during the total overlapping coverage of X-ray and IR coverage, one on 2016 July 12, one on 2016 July 18, and two on 2017 July 15. Increasing p_0 to 0.1 resulted in the detection of five flares (where the narrow peak around 910 min on 2017 July 15 is also identified as an individual flare). Both numbers are consistent with past measurements of the average number of X-ray flares from Sgr A* (~1.1/day; Neilsen et al. 2015; Ponti et al. 2015). The results of the Bayesian Blocks analysis are overplotted on the X-ray light curves in Figure 1. The lowest block in each light curve characterizes the quiescent flux from Sgr A* and had an average count rate of 0.006 counts s^{-1}. All of the X-ray flares detected above this constant thermal emission are relatively faint ($\lesssim$45 total counts) and do not contain enough counts to extract spectral information.

While the X-ray flares are detected as distinct peaks rising above a constant background (which may be hiding fainter
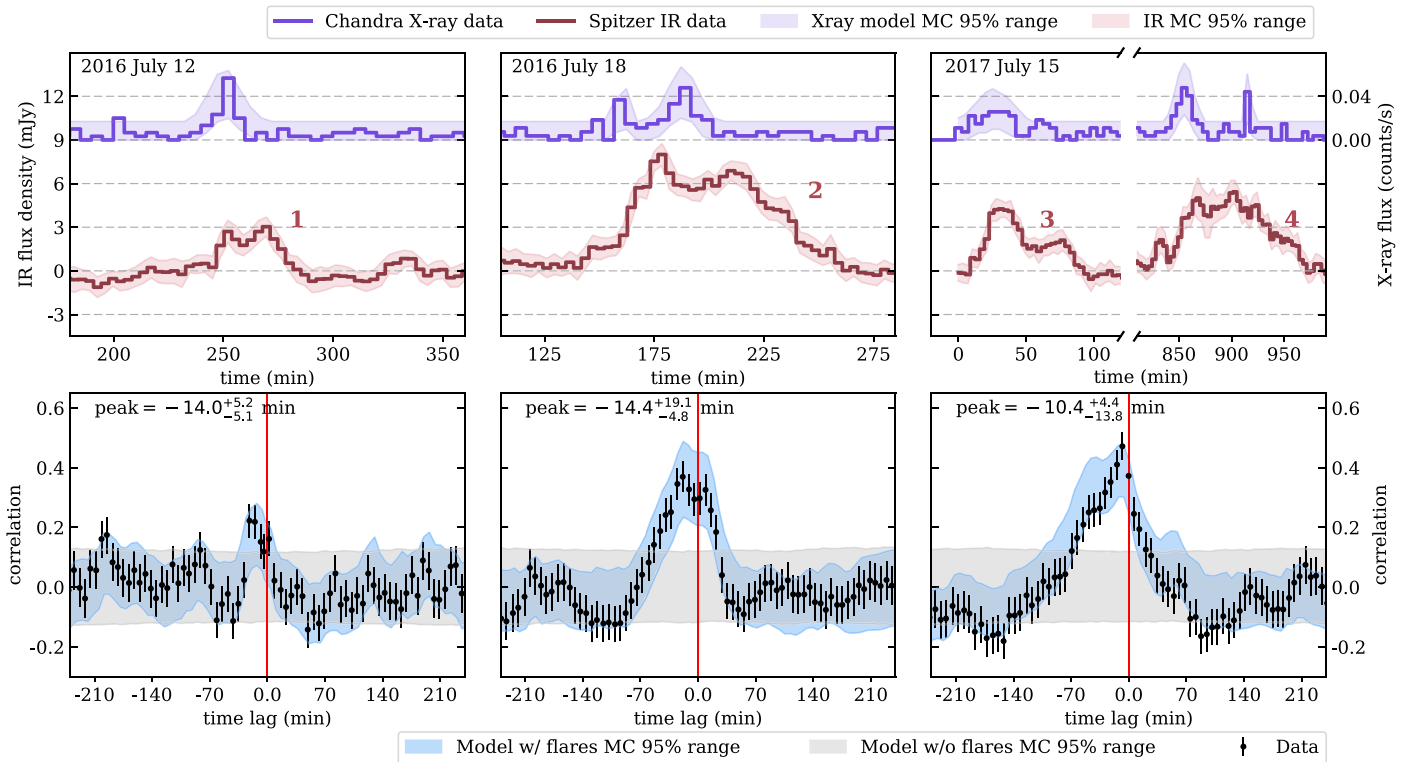
Figure 2. Results from running the `ZDCF` on the three epochs that have X-ray flaring activity. The top row shows the data zoomed in on the portions of the light curves where we see significant X-ray activity. Labels 1–4 indicate the four IR peaks associated with this activity and also marked in Figure 1. X-ray data are displayed in purple with 5 min bins, and IR is displayed in red with 3.5 min bins. Their respective envelopes show the 95% range of the 10,000 Monte Carlo (MC) realizations of the light curves. The third panel (2017 July 15) zooms in on two sections of the light curve. The bottom row shows results of running the z-transform discrete correlation function (`ZDCF`) on the entire ~24 hr light curves for each of the dates in the top panels. The blue envelope is the 95% range of results from running the MC realizations of the X-ray and IR light curves through the `ZDCF`, while the gray envelope is the 95% range of the results of running the IR MC realizations through the `ZDCF` with 10,000 realizations of simulated Poisson noise consistent with the characteristics of the X-ray quiescent emission (no flares). The time lag and 68% confidence interval from running `PLIKE` on the 10,000 MC `ZDCF` results is displayed in the top left corner of these panels. The negative values for the position of the peaks indicate that the X-ray leads the IR.

X-ray variability; Neilsen et al. 2013), the emission from Sgr A* at IR wavelengths is constantly varying. In the three epochs where we observe significant X-ray activity, the IR flux from Sgr A* rises above ~2 mJy within tens of minutes of the peak in the X-ray (see the top row of Figure 2). The IR activity associated with significant X-ray flares appears to rise at the same time as the X-ray but lasts for a longer time ($\mathrm{FWHM_{IR}} \gtrsim 2 \times \mathrm{FWHM_{X\text{-}ray}}$). These longer IR "flares" are labeled 1–4 in Figures 1 and 2, with flares 1–3 roughly associated with the first three X-ray flares and flare 4 associated with both the fourth and fifth X-ray flares identified with the Bayesian Blocks analysis. There are also multiple IR peaks at ~2 mJy where we see no significant X-ray emission (e.g., around minute 300 on 2014 June 2; minute 450 on 2014 July 4; minute 500 and 1300 on 2016 July 18; and minute 900 on 2017 July 25).

3.2. Cross-correlation

To quantify lags between the peaks of potentially associated activity in the X-ray and IR, we used the z-transform discrete correlation function (`ZDCF`; Alexander 1997), a tool that estimates the cross-correlation function without penalty for having a sparse or unevenly sampled light curve. We used the FORTRAN 95 implementation[13] of both the `ZDCF` and the

maximum likelihood function used to estimate the location of the `ZDCF` peak described in Alexander (2013).

The `ZDCF` is not sensitive to the relative amplitudes of the input light curves. This allows us to run the `ZDCF` without renormalizing the *Chandra* and *Spitzer* data. The `ZDCF` *is*, however, sensitive to the shape of the light curves, meaning that two flares with similar rise times, envelopes, and decay times will result in the ZDCF having a stronger correlation with less uncertainty in the time lag. In our case, this means that if a flare in the X-ray light curve has a significantly shorter duration than a coincident flare in the IR light curve, the peak in the `ZDCF` will be weaker and flatter than if they had the same duration, limiting the precision in the measured time lag.

For our analysis we used the 3.5 min binned IR light curves as the first input and the 300 s binned X-ray light curves as the second input. A positive time lag corresponds to a feature in the IR leading the X-ray, and a negative time lag corresponds to a feature in the IR lagging the X-ray. Figure 2 shows the results of running the `ZDCF` on the three epochs for which we detect significant X-ray activity (2016 July 12, 2016 July 18, and 2017 July 15).

To identify significant correlation peaks, we generated 10,000 Monte Carlo (MC) realizations of the X-ray and IR light curves and ran them through the `ZDCF`. These results are visualized as the blue envelope in the bottom row of Figure 2. The X-ray MC realizations were generated by adding Poisson noise to a smooth model containing the Gaussians fit to the

---

[13] www.weizmann.ac.il/weizsites/tal/research/software/

Table 2
Time Lags: *Spitzer/Chandra* Flares

Date	Time Lag (min)	68% Interval	99.7% Interval
2016 Jul 12	$-14.0^{+5.2}_{-5.1}$	(−19.1, −8.8)	(−30.7, +2.8)
2016 Jul 18	$-14.4^{+19.1}_{-4.8}$	(−19.2, +4.7)	(−27.7, +19.2)
2017 Jul 15	$-10.4^{+4.4}_{-13.8}$	(−24.2, −6.0)	(−71.5, +6.4)

Note. Negative values mean X-ray leads IR. Uncertainties on the time lag in the first column span the 68% confidence interval on the 10,000 MC runs. The second column displays the boundaries of this 68% confidence interval, while the third column displays the 99.7% confidence interval.

Figure 3. Histogram of all the time lags measured in our 6000 simulations. The pink shaded region marks the range from −20 to +20 min and the thin red line marks zero time-lag.

flares. The IR realizations were generated from the 3.5 min binned light curves by perturbing each point by a random amount drawn from a Gaussian distribution with standard deviation equal to that of the mean of the ∼25 BCD coadds in the bin. We confirmed that these distributions in the *Spitzer* light curve bins are normal and dominated by white noise (see Witzel et al. 2018). For comparison, we cross-correlated the 10,000 IR MC realizations with a separate set of 10,000 X-ray MC light curves containing *only* Poisson noise at the level of the quiescent flux (no flares, plotted in gray in Figure 2). Significant correlation peaks are those that rise above the gray MC "no flare" envelope. There are correlation peaks near zero time lag in all three epochs. Peaks in the 2016 July 18 and 2017 July 15 epochs are considered significant and the small peak in the 2016 July 12 epoch is considered marginally significant. The highest points in the peak of these correlations all occur at negative time lags, implying that flares in the X-ray may *lead* activity in the IR.

To robustly measure the uncertainty on the time lags, we located the position of the peak in all 10,000 results from ZDCF and defined confidence intervals based on the distribution of these 10,000 time lags. This method for estimating the uncertainties takes the errors on the light curve data into account. Table 2 compiles the time lags and the confidence intervals found in the MC analysis. All three epochs indicate the X-ray emission peaks approximately 10–20 min before the IR flux density peak.

As an alternative analysis to the ZDCF, we also calculated the cross-power spectra of each epoch, but did not find it to show any strong trends or constrain any relevant timing between the two data sets. We also compared the ZDCF to the ccf function in *R*, which yielded almost identical results, but had the disadvantage of requiring the two time series be sampled concurrently and at equally spaced points in time.

4. Discussion

4.1. Are the X-Ray and IR Flares Truly Correlated?

We detected IR activity nearly coincident with every X-ray flare, though not every IR peak with flux density level ≳2 mJy had corresponding X-ray emission (perhaps because the weaker X-ray flares are hidden beneath the blanket of constant thermal emission). To investigate whether or not the observed X-ray and IR variabilities are truly associated, we consider the alternative possibility that the apparently correlated peaks in X-ray and IR emission are a chance association of peaks in typical X-ray and IR variability.

We generated 1000 simulations of each of our six *Spitzer* IR light curves by randomly drawing from the posterior of case 3
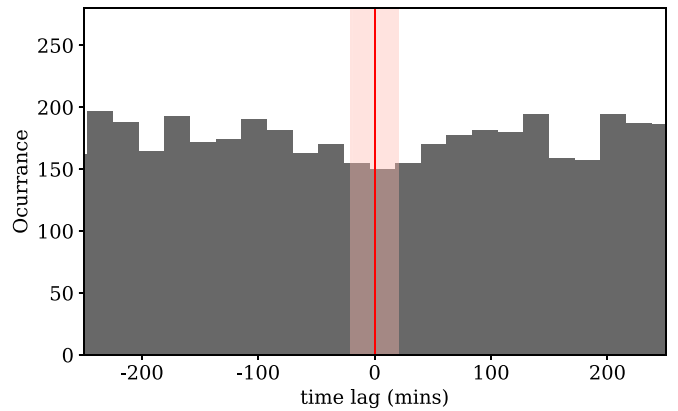
in Witzel et al. (2018), and then producing a random light curve for the given parameter set. The simulated light curves have the measurement noise properties of *Spitzer*, and they are distributed accordingly to the log-normal flux density distribution determined for the *M*-band (4.5 μm). We ran the 1000 simulated light curves for each epoch through the ZDCF with the corresponding *Chandra* X-ray light curves as the second input. This resulted in a total of 6000 cross-correlations between *Chandra* X-ray light curves and simulated *Spitzer* IR light curves.

To test the probability of detecting a time lag similar to the one we measured by chance, we counted the occurrences of significant time lags measured between −20 and 0 min in our 6000 cross-correlations. A detection of a time lag within this window occurred in 138 of our 6000 instances. In other words, given *Chandra* X-ray data and a random *Spitzer* light curve simulating the typical IR variability of Sgr A*, a detection of a time lag between 0 and −20 min arose by chance 2.3% of the time. Increasing the window of coincidence to include positive time lags (−20 min to +20 min) resulted in 279 instances of coincidence, or a 4.7% chance occurrence rate. Figure 3 shows a the distribution of time lags measured in all 6000 simulations. Since we detected a time lag of negative 10–20 min in all three of the real *Spitzer/Chandra* epochs containing significant X-ray flares, we consider this strong evidence that the X-ray and IR flares from Sgr A* are indeed physically connected.

4.2. Comparisons to Previous Work and Flaring Models

There are many models in the literature that attempt to connect Sgr A*'s flares across multiple wavelengths, and particular attention has been paid to the near-simultaneous X-ray and IR peaks. Most models assume the IR peaks are caused by a population of non-thermal electrons emitting synchrotron radiation. Models then evoke synchrotron and/or IC radiation to connect these IR peaks to their corresponding X-ray flares. Figure 4 displays the time lags found by the cross-correlation analysis in this work in the context of lags (or lack thereof) reported in the literature with flares in both X-ray and IR. Most previous observations with overlapping X-ray and IR coverage reported no time lag between flares seen in both wavelengths, using language like "simultaneous to within *x* minutes" but quoting no uncertainties.
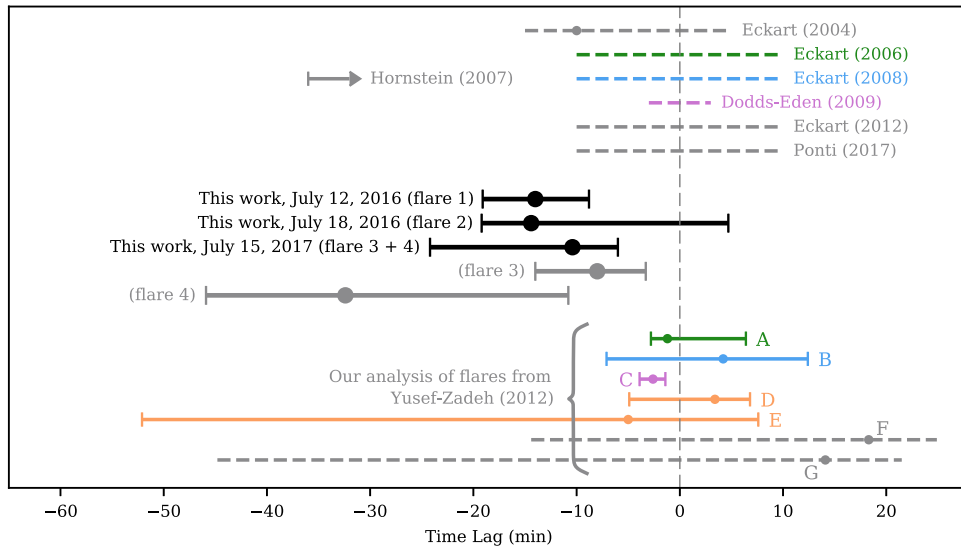
Figure 4. Time lags between IR and X-ray flares as reported in this work and in the literature. Plotted in black are the time lags from the three epochs in this work with significant X-ray and IR activity and their 68% confidence intervals determined from the distribution of 10,000 time lags measured from our MC realizations of our light curves. Plotted in solid gray are the results of the cross-correlation of the isolated sections of the 2017 July 15 light curve containing IR flares 3 and 4. Regions marked with dashed lines come from works that describe the flares to be "simultaneous to within x minutes" but quote no uncertainties (Eckart et al. 2004, 2006a, 2008, 2012; Hornstein et al. 2007; Dodds-Eden et al. 2009; Ponti et al. 2017). For example, Eckart et al. (2004) report an X-ray and IR flare that are simultaneous to within 15 min, so we mark that with a line symmetric around zero ranging from −15 min to 15 min. Several other works report simultaneity between the X-ray and IR peaks, but do not report a time frame within which that claim can be considered valid (Yusef-Zadeh et al. 2006, 2009; Trap et al. 2011). The upper limit from Hornstein et al. (2007) indicates an X-ray flare whose peak occurred 36 min before IR observations began. Yusef-Zadeh et al. (2012) is the only work to report any time lag between the X-ray and IR with error bars. We re-analyze the seven flares presented in their work and plot the results of our re-analysis here. Five of these flares come from previously reported data sets (color coded as green, blue, magenta, and orange for Eckart et al. 2006a, 2008; Dodds-Eden et al. 2009; and Yusef-Zadeh et al. 2009 respectively) and two come from a previously unreported data set (plotted in gray). The significance of the X-ray flares in these last two data sets is very low (see Section 4.3).

Table 3
Time Lags: Yusef-Zadeh et al. (2012) Flares

Flare	Date	Orig. Paper	IR Facility	X-Ray Facility	YZ Time Lag (min)	Our Time Lag (min)
A	2004 Jul 6/7	Eck+2006b	VLT (K band)	*Chandra*	$7^{+1.3}_{-1.2}$	$-1.2^{+7.6}_{-1.6}$
B	2005 Jul 30	Eck+2008	VLT (K band)	*Chandra*	$8^{+10}_{-10.1}$	$4.2^{+8.2}_{-11.3}$
C	2007 Apr 4	DE+2009	VLT (K band)	*Chandra*	$-0.5^{+7}_{-6.5}$	$-2.6^{+1.2}_{-1.3}$
D	2007 Apr 4	YZ+2009	*HST*/NICMOS	*XXM-Newton*	$5^{+1}_{-1.4}$	$3.4^{+3.4}_{-8.3}$
E	2007 Apr 4	YZ+2009	*HST*/NICMOS	*XXM-Newton*	$5.0^{+1.9}_{-1.5}$	$-5.0^{+12.6}_{-47.1}$
F	2008 May 5	YZ+2012	VLT (K band)	*Chandra*	$19^{+6.8}_{-2.4}$	$18.3^{+6.6}_{-32.7}$
G	2008 Jul 26/27	YZ+2012	VLT (K band)	*Chandra*	$14.6^{+5.6}_{-7.4}$	$14.1^{+7.4}_{-58.9}$

Note. Negative values mean X-ray leads IR. The first column labels the flares. The second column lists the date the simultaneous data were taken. Column three lists the original paper where the data were reported (Eck+2006b = Eckart et al. 2006a, Eck+2008 = Eckart et al. 2008, DE+2009 = Dodds-Eden et al. 2009, YZ +2009 = Yusef-Zadeh et al. 2009, YZ+2012 = Yusef-Zadeh et al. 2012). Columns four and five list the facilities with which the IR and X-ray data were collected. Column six lists the time lag and 1σ errors reported from the ZDCF analysis in Yusef-Zadeh et al. (2012). The last column lists the time lags and 68% confidence intervals we find from our Monte Carlo analysis (10,000 realizations).

4.2.1. Synchrotron

In models where both the IR and X-ray emission are produced through direct synchrotron radiation, the population of electrons responsible for the emission would have very high energies ($\gamma \gtrsim 10^5$), and the cooling timescale would be much shorter than the duration of a typical X-ray flare. This requires that the energized electrons have a sustained source over the duration of the flare (Baganoff et al. 2001; Markoff et al. 2001; Yuan et al. 2004; Ponti et al. 2017). Such processes often predict a simultaneous rise in the X-ray and IR flares, with the higher-energy X-rays fading faster as the electrons lose energy through synchrotron cooling and/or adiabatic expansion (e.g., Dodds-Eden et al. 2010). These predictions from pure

synchrotron models are consistent with our tentative measurement of a time lag between the peak in the X-rays and a peak in the IR (equivalently, the X-ray flare rising with the IR but falling faster). Alternatively, if the IR emission is characterized by a number of "subpeaks" then the X-ray flare could be coincident with an individual subpeak. This could lead to an offset between the X-ray peak and the centroid of the broader IR envelope.

Two studies with observations of simultaneous X-ray and IR flares (Dodds-Eden et al. 2009; Ponti et al. 2017) found the X-ray flares to be consistent with synchrotron radiation. They reported particularly bright X-ray flares coincident with IR peaks where the IR rise had already begun when the X-ray flux rose, and the X-ray flare fell before the IR peak ended. Both of
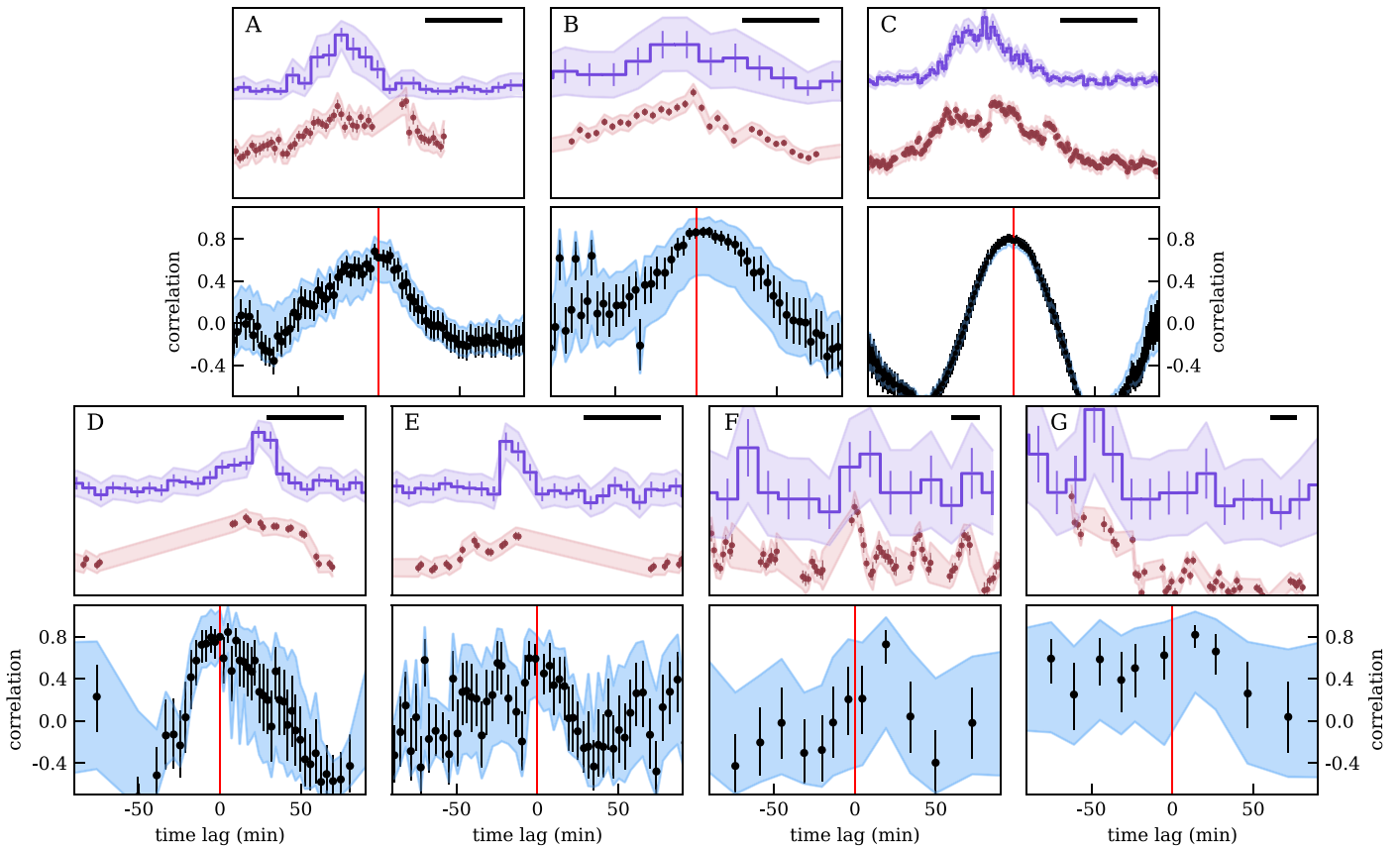
Figure 5. X-ray and IR light curves discussed in Yusef-Zadeh et al. (2012) and the cross-correlations we find in our MC analysis. First and third row panels display the light curves along with the 95% envelopes of our MC realizations generated by drawing from a normal distribution centered around the true data with a standard deviation proportional to the errors on the light curves. Symbols and line styles are identical to those in Figure 2. For this visualization, the *y*-scales are arbitrary, and the black line in the upper right of each white panel indicates a 30 min interval. The results of the ZDCF on the real light curves are displayed in black in the corresponding lower panels, while the MC envelope from which the time lags are measured is displayed in blue. The resulting time lags and confidence intervals are reported in column five of Table 3 and plotted in Figure 4. Table 3 lists the dates, original papers, and facilities from which the IR and X-ray light curves come. All X-ray light curves were binned at 300 s except for F and G, which were binned at 1500 s. IR light curves A, B, and C were binned at 140 s, while light curves D and E were binned at 144 s and light curves F and G were binned at 120 s.

these studies used measurements of the spectral indices of the flares to argue that a synchrotron emission mechanism with a cooling break was responsible for both the IR and X-ray flares. The simultaneous X-ray and IR peaks of Dodds-Eden et al. (2009) were again interpreted by Dodds-Eden et al. (2010) in the context of synchrotron emission due to accelerated electrons from magnetic reconnection, and Li et al. (2017) re-interpreted the data in the context of magnetic reconnection accelerating electrons in the coronal region rather than the main body of the accretion flow.

During a low flux density phase of activity, Witzel et al. (2018) measured the spectral index of the *Spitzer* IR measurements to be significantly redder than typically observed at high flux densities. Using this measurement as a constraint, they determined that the majority of NIR variability data is consistent with a variable spectral index that linearly depends on the logarithm of flux density. Both this determination of the variable IR spectral index for a large sample of variability data and the individual multi-wavelength flare analyses in Dodds-Eden et al. (2010) and Ponti et al. (2017) suggest synchrotron mechanisms, which also dominate the submm to IR, and at times reach energies high enough to cause X-ray flares. Indeed, the unchanging spectral index of X-ray variability at high energies is also consistent with a synchrotron scenario (Zhang et al. 2017).

4.2.2. Synchrotron Self-Compton

In the scenario where the electrons responsible for IR synchrotron radiation are accelerated to energies of $\gamma \sim 100$–1000, they could scatter the synchrotron IR photons up to X-ray energies through SSC, predicting near simultaneity for the flares. Electrons of these energies in a magnetic field with a strength typically assumed for the accretion flow around Sgr A* would have synchrotron cooling timescales on the order of hours, which fits the duration of the strongest X-ray flares observed in other works (e.g., Eckart et al. 2008; Dodds-Eden et al. 2009; Ponti et al. 2017, D. Haggard et al. 2018 in preparation). Several authors have modeled the flares as a SSC process (e.g., Markoff et al. 2001; Eckart et al. 2004, 2006a, 2008; Trap et al. 2011; Dibi et al. 2014).

Two of these studies (Eckart et al. 2006a, 2008) reported an X-ray and IR flare to be simultaneous to within 10 min. Eckart et al. (2006a) used this simultaneity and the suggestion that the IR flare spectrum is relatively red with a variable spectral index (e.g., Eisenhauer et al. 2005; Witzel et al. 2018) to argue in favor of the SSC picture. Eckart et al. (2008) observed a polarized IR flare with an X-ray counterpart. They also found that the flares fit the SSC picture of submm synchrotron photons being up-scattered to IR and X-ray wavelengths and discussed this in the context of a model involving a temporary
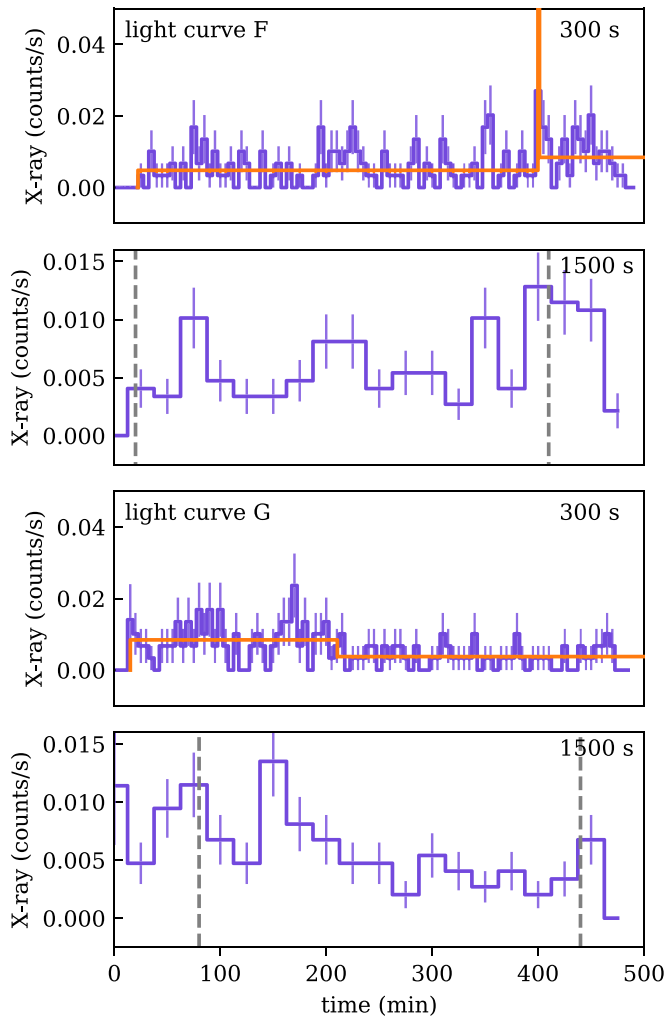
Figure 6. Sgr A* X-ray light curves extracted from *Chandra* ObsID 9169 (light curve F) and ObsID 9173 (light curve G). Top: light curves with 300 s binning. Orange displays the Bayesian Blocks results with $p_0 = 0.1$. Bottom: light curves with 1500 s (25 min) binning. Gray dashed lines indicate the same interval analyzed by Yusef-Zadeh et al. (2012).

4.2.3. Inverse Compton

In IC models connecting the IR and X-ray variability, IR-synchrotron emitting electrons with energies $\gamma \sim 100$–1000 scatter submm seed photons up to X-ray energies, predicting a potential lag in the X-rays relative to the IR outburst. This is inconsistent with our measurement of a negative X-ray time lag, which illustrates (at least tentatively) that the X-rays *lead* the IR or, at the very least, rise simultaneously and fall faster.

Yusef-Zadeh et al. (2006, 2009) detected several faint X-ray flares with IR counterparts, but quoted no uncertainty on any time lag. Yusef-Zadeh et al. (2006) predicted that in the IC scenario, the spectral index of an IR flare must be the same as the correlated X-ray flare (i.e., $\alpha \sim 0.6$). Unfortunately, the X-ray flare they observed did not contain enough counts to provide any spectral information. In their campaign to observe Sgr A* across many wavelengths (cm, mm, submm, IR, X-ray), Yusef-Zadeh et al. (2009) also argued in favor of an IC model, but one in which synchrotron IR photons are up-scattered to X-ray wavelengths by electrons responsible for the radio and submm emission of Sgr A*.

As the only other work to quote uncertainties on the time lags found in their cross-correlations, Yusef-Zadeh et al. (2012) re-analyzed archival data (Eckart et al. 2006a, 2008; Yusef-Zadeh et al. 2006, 2009; Dodds-Eden et al. 2009) along with previously unreported observations. They reported evidence for the peak of the X-ray flares *lagging* the IR peaks with a time delay ranging from a few to tens of minutes. Assuming there is not more than one population of flares, this is in tension with our finding of the X-rays tentatively *leading* the IR. These authors also employed the ZDCF, and the time lags they find are quoted in Table 3.

4.3. Re-analyzing Light Curves from the Literature

Due to the very low signal-to-noise in the individual cross-correlation results and the large binning of some of the X-ray data in Yusef-Zadeh et al. (2012), we suspect their reported 1σ error bars to be underestimated. For these reasons, we elected to run their light curves through our cross-correlation and MC analysis to verify their results, provide us with a consistent comparison, and determine the effect that the signal-to-noise ratio of a flare has on the cross-correlation.

Using the seven light curves presented in Yusef-Zadeh et al. (2012), we performed a cross-correlation analysis identical to the analysis we applied to our own light curves in Section 3.2. We generated 10,000 MC instances of the light curves scaled in proportion to the errors on the data and ran the ZDCF on them. The mean of the resulting distribution of time lags was adopted as our measurement, with uncertainties determined by the interval within which 68% of the time lags fall. Table 3 labels the flares A to G and displays the time lags and 1σ errors reported by Yusef-Zadeh et al. (2012) as well as the time lags and uncertainties that we measure from our MC analysis. Figure 5 re-plots the light curves found in their work (with the exception of Flare C, which is not plotted by Yusef-Zadeh et al. 2012 but still included in their analysis) along with the results of our MC analysis with the ZDCF. Figure 4 displays our measurements for these seven flares in the context of this work and the literature.

The differences between our results and those reported by Yusef-Zadeh et al. (2012) are due to our MC analysis incorporating the signal-to-noise of the input light curves. In

disk and a short jet, where rotating spots in the disk are responsible for variations in the IR flares.

Eckart et al. (2004) reported a possible time lag of ∼10 min between the first flares detected in simultaneous observations, with the X-ray leading the IR. Due to the large binning of their X-ray light curves they quote ∼15 min as a conservative upper limit for any time lag. They describe the flares with a SSC model in which IR flares are due to both synchrotron and the up-scattering of synchrotron submm photons, and X-ray flares are produced through the IC scattering of submm and IR photons.

Finally, reporting no constraints on the simultaneity of the X-ray and IR variability in their work, Trap et al. (2011) interpreted their X-ray/IR/submm data in the context of a model involving an expanding plasmoid releasing synchrotron submm and IR radiation and up-scattering to X-ray energies through SSC processes. These models are often invoked to explain the tentative time lags between the X-ray/IR flares and submm or radio activity. The authors found that the simplest version of this expanding plasmoid model did not adequately explain their data.

a light curve with low signal-to-noise, larger uncertainties on the data points will produce MC simulations that span a larger flux range, resulting in a broader range of time lags found between features in the light curves. Both methods employ the `ZDCF`, but while Yusef-Zadeh et al. (2012) quote the time lag of a single `ZDCF/PLIKE` run, we measure the time lag and estimate the uncertainties from 10,000 runs of the `ZDCF`.

In comparison to Yusef-Zadeh et al. (2012), this method estimates larger and more realistic uncertainties on the time lags for flares A, D, E, F, and G, similar uncertainties for flare B, and a smaller uncertainty for the time lag of flare C, the brightest simultaneous X-ray and IR flare observed to date (Dodds-Eden et al. 2009). Our analysis of flares A, C, D, and E found the time lag to be closer to zero or even negative compared to the lag reported by Yusef-Zadeh et al. (2012). The low signal-to-noise in the light curves of flares E, F and G is reflected in the poor constraints on a time-lag.

In the case of flares F and G, we question whether cross-correlating these X-ray light curves binned at 25 min with IR light curves binned at 2 min is meaningful. To test the variability of the light curves containing flares F and G, we opted to download the raw *Chandra* data and run the flare detection algorithm we used for our X-ray light curves (Bayesian Blocks algorithm; see Section 3.1). The data are found within *Chandra* ObsIDs 9169 and 9173. Figure 6 plots the results of running the Bayesian Blocks flare detection algorithm on light curves F and G, the lowest signal-to-noise light curves in Figure 5. In our Bayesian Blocks analysis of these light curves (orange lines in Figure 6), we do not detect any statistically significant X-ray peaks near the IR flares discussed by Yusef-Zadeh et al. (2012). The cross-correlations for these observations should therefore not be considered measurements of meaningful lags between IR and X-ray variability.

5. Conclusion

We have presented results based on new observations which are the longest simultaneous IR and X-ray observations of Sgr A* to date. These overlapping light curves offer the best tests of the connection between these two wavelengths, and provide a crucial probe of Sgr A*'s variable emission. We detect four X-ray flares ($\sim 4\times$ quiescence) and no "strong" X-ray flares ($\geqslant 10\times$ quiescence) during the combined >100 hr that *Chandra* observed Sgr A*. The IR emission of Sgr A* showed peaks coinciding with the weak X-ray flares and also occurring at times when no X-ray flares are detectable. A cross-correlation analysis of all our simultaneous light curves suggests that the X-ray flares may *lead* the IR by approximately 10–20 min, but the 99.7% confidence intervals are still consistent with zero time-lag. This is in agreement with models that describe both the X-ray and IR flares as synchrotron emission originating from particle acceleration events involving magnetic reconnection and shocks in the accretion flow (e.g., see 4.1 of Dodds-Eden et al. 2010) and consistent with models that predict simultaneity of the flares through SSC processes. Our results are inconsistent with models invoking external populations of electrons through IC processes as described by Yusef-Zadeh et al. (2012), though it is not obvious that all X-ray/IR flares are produced by the same process.

It remains difficult to distinguish between the suggested flaring mechanisms connecting the X-ray and IR. Despite having the longest uninterrupted and simultaneous X-ray/IR data set of Sgr A* to date, we observed no bright X-ray flares during the 4+ days of observations reported here. Though this prevented us from gaining spectral information from the faint X-ray flares, future coordinated observations may catch significantly brighter simultaneous outbursts as has happened in the past (Dodds-Eden et al. 2009) and will certainly add to the growing statistical strength of the catalog of multi-wavelength flares. Previous observations have revealed sub-structure in the outbursts of both wavelengths (e.g., Dodds-Eden et al. 2009, D. Haggard et al. 2018, in preparation), and future observations of bright simultaneous outbursts could allow for a more detailed cross-correlation of sub-components in the X-ray and IR peaks.

In the immediate future, upcoming *Spitzer*/*Chandra* observations approved for the summer of 2019[14] may detect multiple bright flares, which may be key to constraining the time lag between the X-ray and the IR. In the longer term, a better understanding of the time-dependent emission from Sgr A* will allow for the characterization of the accretion physics around the black hole and inform the next generation of GRMHD simulations. Not only will long epochs of observations at multiple wavelengths be ideal data sets for distinguishing between semi-analytical flaring models, but Sgr A*'s variability will provide a strict benchmark for testing whether or not state-of-the-art simulations are probing the real physical scales of the turbulent accretion flow. Additionally, the multi-wavelength efforts coordinated with the Event Horizon Campaigns in April 2017 and 2018 hold promise for narrowing in on the physical processes that drive Sgr A*'s variability.

Facilities: Spitzer/IRAC, *Chandra*/ACIS.

Software: CIAO Fruscione et al. (2006), NumPy (Jones et al. 2015), AstroPy (The Astropy Collaboration et al. 2018), Matplotlib (Hunter 2007), Bayesian Blocks (Williams et al. 2017), ZDCF (Alexander 2013).

ORCID iDs

H. Boyce ⓘ https://orcid.org/0000-0002-6530-5783
D. Haggard ⓘ https://orcid.org/0000-0001-6803-2138
G. Witzel ⓘ https://orcid.org/0000-0003-2618-797X

---

[14] https://www.cfa.harvard.edu/irac/gc/

S. P. Willner ⓘ https://orcid.org/0000-0002-9895-5758
J. Neilsen ⓘ https://orcid.org/0000-0002-8247-786X
J. L. Hora ⓘ https://orcid.org/0000-0002-5599-4650
S. Markoff ⓘ https://orcid.org/0000-0001-9564-0876
G. G. Fazio ⓘ https://orcid.org/0000-0002-0670-0708
P. Lowrance ⓘ https://orcid.org/0000-0001-8014-0270
M. R. Morris ⓘ https://orcid.org/0000-0002-6753-2066

References

Alexander, T. 1997, in Astronomical Time Series, Vol 218, ed. D. Maoz, A. Sternberg, & E. M. Leibowitz (Dordrecht: Kluwer), 163
Alexander, T. 2013, arXiv:1302.1508
Baganoff, F. K., Bautz, M. W., Brandt, W. N., et al. 2001, Natur, 413, 45
Baganoff, F. K., Maeda, Y., Morris, M., et al. 2003, ApJ, 591, 891
Ball, D., Özel, F., Psaltis, D., & Chan, C.-K. 2016, ApJ, 826, 77
Barrière, N. M., Tomsick, J. A., Baganoff, F. K., et al. 2014, ApJ, 786, 46
Boehle, A., Ghez, A. M., Schödel, R., et al. 2016, ApJ, 830, 17
Bremer, M., Witzel, G., Eckart, A., et al. 2011, AAP, 532, A26
Čadež, A., Calvani, M., & Kostić, U. 2008, AAP, 487, 527
Capellupo, D. M., Haggard, D., Choux, N., et al. 2017, ApJ, 845, 35
Chan, C.-K., Psaltis, D., Özel, F., et al. 2015, ApJ, 812, 103
Coti Zelati, F., Rea, N., Papitto, A., et al. 2015, MNRAS, 449, 2685
Coti Zelati, F., Rea, N., Turolla, R., et al. 2017, MNRAS, 471, 1819
Dexter, J., Agol, E., & Fragile, P. C. 2009, ApJL, 703, L142
Dibi, S., Markoff, S., Belmont, R., et al. 2014, MNRAS, 441, 1005
Dibi, S., Markoff, S., Belmont, R., et al. 2016, MNRAS, 461, 552
Dodds-Eden, K., Gillessen, S., Fritz, T. K., et al. 2011, ApJ, 728, 37
Dodds-Eden, K., Porquet, D., Trap, G., et al. 2009, ApJ, 698, 676
Dodds-Eden, K., Sharma, P., Quataert, E., et al. 2010, ApJ, 725, 450
Doeleman, S. S., Weintroub, J., Rogers, A. E. E., et al. 2008, Natur, 455, 78
Eckart, A., Baganoff, F. K., Morris, M., et al. 2004, AAP, 427, 1
Eckart, A., Baganoff, F. K., Schödel, R., et al. 2006a, AAP, 450, 535
Eckart, A., Baganoff, F. K., Zamaninasab, M., et al. 2008, AAP, 479, 625
Eckart, A., García-Marín, M., Vogel, S. N., et al. 2012, AAP, 537, A52
Eckart, A., Schödel, R., Meyer, L., et al. 2006b, AAP, 455, 1
Eisenhauer, F., Genzel, R., Alexander, T., et al. 2005, ApJ, 628, 246
Fazio, G. G., Hora, J. L., Allen, L. E., et al. 2004, ApJS, 154, 10
Fazio, G. G., Hora, J. L., Witzel, G., et al. 2018, ApJ, 864, 58
Fruscione, A., McDowell, J. C., Allen, G. E., et al. 2006, Proc. SPIE, 6270, 62701V
Genzel, R., Eisenhauer, F., & Gillessen, S. 2010, RvMP, 82, 3121
Genzel, R., Schödel, R., Ott, T., et al. 2003, Natur, 425, 934
Ghez, A. M., Wright, S. A., Matthews, K., et al. 2004, ApJL, 601, L159
Gillessen, S., Plewa, P. M., Eisenhauer, F., et al. 2017, ApJ, 837, 30
Hora, J. L., Witzel, G., Ashby, M. L. N., et al. 2014, ApJ, 793, 120
Hornstein, S. D., Matthews, K., Ghez, A. M., et al. 2007, ApJ, 667, 900
Hunter, J. D. 2007, CSE, 9, 90
Jones, E., Oliphant, T., Peterson, P., et al. 2015, Guide to NumPy (Scotts Valley, CA: CreateSpace Independent Publishing Platform)
Kostić, U., Čadež, A., Calvani, M., & Gomboc, A. 2009, AAP, 496, 307
Li, Y.-P., Yuan, F., & Wang, Q. D. 2017, MNRAS, 468, 2552
Li, Y.-P., Yuan, F., Yuan, Q., et al. 2015, ApJ, 810, 19

Liu, S., & Melia, F. 2002, ApJL, 566, L77
Liu, S., Petrosian, V., & Melia, F. 2004, ApJL, 611, L101
Maitra, D., Markoff, S., & Falcke, H. 2009, AAP, 508, L13
Markoff, S., Falcke, H., Yuan, F., & Biermann, P. L. 2001, AAP, 379, L13
Marrone, D. P., Baganoff, F. K., Morris, M. R., et al. 2008, ApJ, 682, 373
Marrone, D. P., Moran, J. M., Zhao, J.-H., & Rao, R. 2006, ApJ, 640, 308
Marrone, D. P., Moran, J. M., Zhao, J.-H., & Rao, R. 2007, ApJL, 654, L57
Meyer, L., Do, T., Ghez, A., et al. 2008, ApJL, 688, L17
Meyer, L., Eckart, A., Schödel, R., et al. 2006, AAP, 460, 15
Meyer, L., Schödel, R., Eckart, A., et al. 2007, AAP, 473, 707
Morris, M. R., Meyer, L., & Ghez, A. M. 2012, RAA, 12, 995
Mossoux, E., Grosso, N., Bushouse, H., et al. 2016, AAP, 589, A116
Neilsen, J., Markoff, S., Nowak, M. A., et al. 2015, ApJ, 799, 199
Neilsen, J., Nowak, M. A., Gammie, C., et al. 2013, ApJ, 774, 42
Nowak, M. A., Neilsen, J., Markoff, S. B., et al. 2012, ApJ, 759, 95
Ponti, G., De Marco, B., Morris, M. R., et al. 2015, MNRAS, 454, 1525
Ponti, G., George, E., Scaringi, S., et al. 2017, MNRAS, 468, 2447
Quataert, E. 2002, ApJ, 575, 855
Reid, M. J., & Brunthaler, A. 2004, ApJ, 616, 872
Scargle, J. D. 1998, ApJ, 504, 405
Scargle, J. D., Norris, J. P., Jackson, B., & Chiang, J. 2013, ApJ, 764, 167
Shahzamanian, B., Eckart, A., Valencia, S. M., et al. 2015, AAP, 576, A20
Shcherbakov, R. V., Penna, R. F., & McKinney, J. C. 2012, ApJ, 755, 133
The Astropy Collaboration, Price-Whelan, A. M., Sipőcz, B. M., et al. 2018, arXiv:1801.02634
Trap, G., Goldwurm, A., Dodds-Eden, K., et al. 2011, AAP, 528, A140
Trippe, S., Paumard, T., Ott, T., et al. 2007, MNRAS, 375, 764
van der Laan, H. 1966, Natur, 211, 1131
Wang, Q. D., Nowak, M. A., Markoff, S. B., et al. 2013, Sci, 341, 981
Weisskopf, M. C., Tananbaum, H. D., Van Speybroeck, L. P., & O'Dell, S. L. 2000, Proc. SPIE, 4012, 2
Werner, M. W., Roellig, T. L., Low, F. J., et al. 2004, ApJS, 154, 1
Williams, P. K. G., Clavel, M., Newton, E., & Ryzhkov, D. 2017, pwkit: Astronomical Utilities in Python, Astrophysics Source Code Library, ascl:1704.001
Witzel, G., Eckart, A., Bremer, M., et al. 2012, ApJS, 203, 18
Witzel, G., Eckart, A., Buchholz, R. M., et al. 2011, AAP, 525, A130
Witzel, G., Martinez, G., Hora, J., et al. 2018, ApJ, 863, 15
Witzel, G., Morris, M., Ghez, A., et al. 2014, in IAU Symp. 303, The Galactic Center: Feeding and Feedback in a Normal Galactic Nucleus, ed. L. O. Sjouwerman, C. C. Lang, & J. Ott (Cambridge: Cambridge Univ. Press), 274
Xu, Y.-D., Narayan, R., Quataert, E., Yuan, F., & Baganoff, F. K. 2006, ApJ, 640, 319
Younsi, Z., & Wu, K. 2015, MNRAS, 454, 3283
Yuan, F., Quataert, E., & Narayan, R. 2003, ApJ, 598, 301
Yuan, F., Quataert, E., & Narayan, R. 2004, ApJ, 606, 894
Yusef-Zadeh, F., Bushouse, H., Dowell, C. D., et al. 2006, ApJ, 644, 198
Yusef-Zadeh, F., Bushouse, H., Schödel, R., et al. 2015, ApJ, 809, 10
Yusef-Zadeh, F., Bushouse, H., Wardle, M., et al. 2009, ApJ, 706, 348
Yusef-Zadeh, F., Wardle, M., Cotton, W. D., Heinke, C. O., & Roberts, D. A. 2007, ApJL, 668, L47
Yusef-Zadeh, F., Wardle, M., Dodds-Eden, K., et al. 2012, AJ, 144, 1
Zhang, S., Baganoff, F. K., Ponti, G., et al. 2017, ApJ, 843, 96
Zubovas, K., Nayakshin, S., & Markoff, S. 2012, MNRAS, 421, 1315